# Attempts at seismic characterization of a deepwater turbidite channel in Taranaki Basin, New Zealand

Satinder Chopra[1*], Ritesh Kumar Sharma[1], Kurt J. Marfurt[2], Heather Bedle[2], and Sumit Verma[3].

**Abstract**

The deepwater Taranaki Basin located off the northwest coast of New Zealand has considerable potential for big hydrocarbon discoveries, though the country has decided to stop all new offshore exploration to address climate change. The challenge is to determine the presence, distribution, and quality of turbidite reservoirs in the giant Late Miocene channel complex that runs through the deepwater basin. We use seismic attributes and a seismic geomorphology driven workflow that maps individual architectural elements of the channel system and allows us to predict facies that have the potential to be good reservoirs. Data conditioning to balance the spectrum provides significant improvement in not only vertical but also lateral resolution of the channel complex. We show that attributes computed from frequency-balanced data better delineate the finer features in the channel complex. Some attribute combinations can be readily combined through multi-attribute visualization to better map the reservoir architectural elements. Other attributes can be effectively combined for seismic facies classification using unsupervised machine learning application including self-organizing mapping (SOM) and generative topographic mapping (GTM). We find that improving the data bandwidth through frequency balancing improves not only the resolution of attributes by themselves, but also when combined using machine learning.

## Introduction

Deepwater turbidite reservoirs hold some of the largest petroleum reservoirs and thus are important exploration targets. Deepwater turbidite reservoirs occur in the more distal reaches of the system where the suspended sediments are often very well sorted by their grain size, resulting in high porosity. In the absence of well control, prediction of lithology is based on our understanding of the environment of deposition. By identifying and mapping the diverse architectural elements of the turbidite system and placing them within the correct geologic framework, a skilled interpreter can predict which components of the system are more likely sand or shale prone. Seismic data and seismic attributes also provide insight into the connectivity or compartmentalization of different parts of the reservoir (e.g., Deptuck, 2003; Braccini et al., 2011; Reijenstein et al., 2011) which can be used to estimate the number of wells needed to drain the reservoir.

The deepwater Taranaki Basin located off the northwest coast of New Zealand (Figure 1) is covered by several high-quality 3D seismic surveys that have been made available to the public by the New Zealand Petroleum Ministry. The Romney prospect in this basin has a closure area of 200 km$^2$ in 1600 m of water depth and it has been estimated to contain 1100-1650 million barrels of oil-in-place or 1.7 to 2.7 TCF of gas (Uruski and Clark, 2009). Although drilling in New Zealand is currently on hold as part of their effort to mitigate climate change, the release of the data to the public has resulted in the Taranaki Basin being one of the most widely studied basins in the world.

When 3D seismic data image the complex internal geometries of channel systems as they do in this survey, they provide an important resource for studying channel fills and their associated lateral distribution patterns. Li et al. (2017) demonstrated the application of sweetness and coherence attributes interpreted in a seismic geomorphology context and facilitated the geological interpretation of the Late Miocene deepwater channel complex as seen on the Romney 3D seismic volume. This application led to the observation of four channel elements, namely, point bars, migration of channel meander loops, channel erosion and cutting, and avulsion. We showcase our attempts at characterization of this deepwater channel complex in terms of seismic attribute applications, specifically using the unsupervised machine learning seismic facies classification techniques. Features such as levees, channel-fill and overbank deposits appear are more clearly defined on composite seismic attribute displays than on any single attribute by itself. In this study we attempt at providing

[1] SamiGeo, Calgary | [2] The University of Oklahoma | [3] UT Permian Basin
[*] Corresponding author, E-mail: Satinder.Chopra@samigeo.com
DOI: xxx

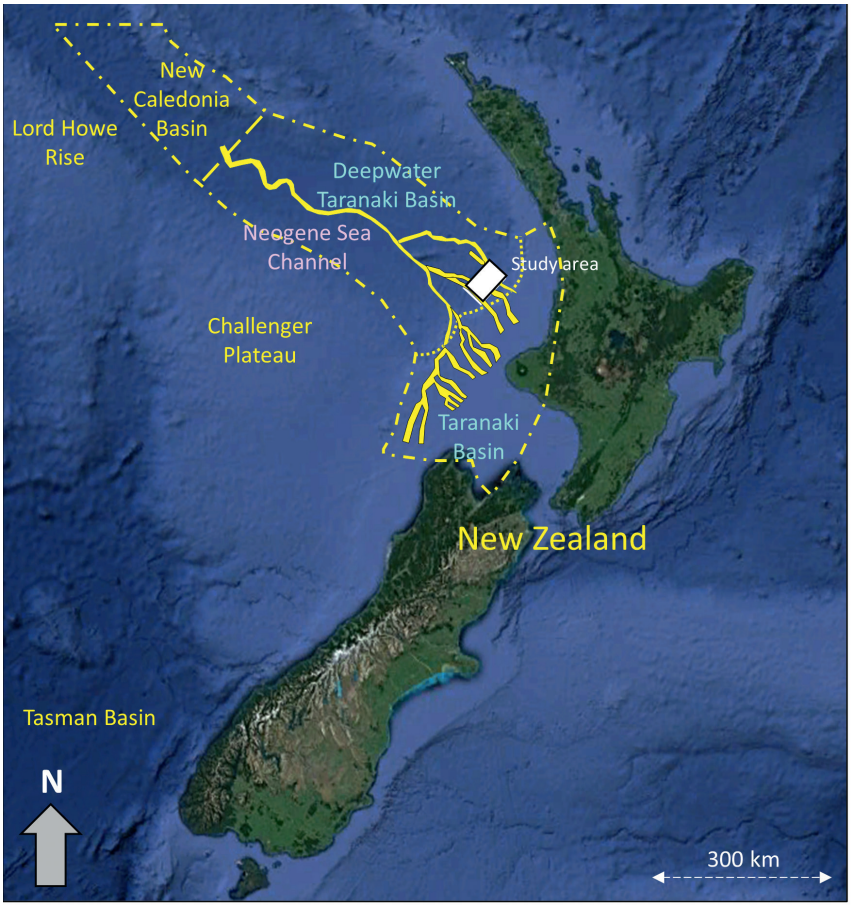


**Figure 1** Location map showing the Deepwater Taranaki Basin lying off the northwest coast of New Zealand. The white rectangle represents the study area. *(Channel outline adapted after Grahame, 2015) Map courtesy Google Earth Pro.*

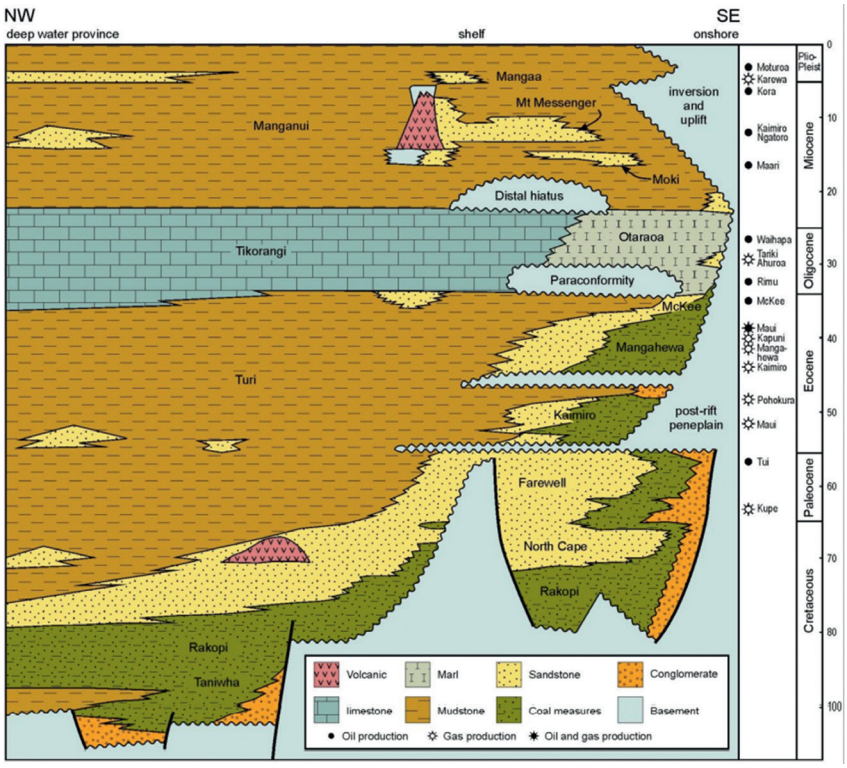


**Figure 2** Stratigraphy of the Taranaki Basin, New Zealand. (After Strogen et al., 2012).

a detailed description of the turbidite facies and their geometry to facilitate a better understanding of the channel architecture.

Only one well is drilled in the area and falls over the seismic volume but does not intersect the Miocene channel. However, this well provides critical lithologic information. The lack of additional well control precludes a quantitative interpretation; for this reason, our interpretation is based on the seismic response to the subsurface and our understanding of geologic processes.

## Geologic background

The deepwater Taranaki Basin developed as a result of multiple tectonic cycles that included the Mesozoic rifting, Late Cretaceous and Paleogene subsidence associated with seafloor spreading, and large-scale Neogene channel systems which transported excessive amounts of sediments into deeper water areas. Figure 2 shows the stratigraphy of the Taranaki Basin and neighbouring areas.

The existing evidence and basin models calibrated to the adjacent shallower water Taranaki Basin wells suggest that the expulsion of petroleum from the deepest parts of the basin began in Late Cretaceous and continues even today (Sherwood, 2002). Consequently, rocks older than 100 Ma are considered to be the geologic basement. The Gondwana breakup from Early to Late Cretaceous initiated the development in the basement that started with the opening of the Tasman Sea associated with the subduction of the Pacific plate along the eastern Gondwana margin. Coal-rich formations were deposited from the Cretaceous to the Paleogene in shallow and non-marine environments, which represent the source rocks in Taranaki Basin (Uruski et al., 2003). The Late Cretaceous to Early Pliocene periods also saw the deposition of sandstone formations because of widespread marine transgression, which was followed by marine silts and muds. The marine shales deposited during Early Cretaceous, and Paleocene periods provide additional source rocks (Strogen et al., 2012). The mudstone deposition took place from Cretaceous to Eocene (Turi Formation) as well as during the Miocene (Manganui Formation) period. These mudstones and the Oligocene to Miocene Tikorangi Formation carbonates (when not fractured) are believed to provide a seal to the source rocks.

Significant uplift of the New Zealand North Island landmass occurred throughout Miocene, and coupled with climate-driven erosion, led to the development of the Neogene major submarine system that transported large volumes of sediment from onshore areas through the deepwater Taranaki Basin into the southern margins of the New Caledonia Basin (Figure 1).

## Available seismic data

The available seismic data were the Romney 3D survey acquired by Anadarko New Zealand in 2011 made publicly available by New Zealand Petroleum and Minerals. We analyse a 700 km$^2$ subset that falls in water depths exceeding 1000 m. The bin size for the data is 12.5 x 25 m, with a sample interval of 4 ms. Although the Romney-1 exploration well was drilled to a depth of 4575 m below sea surface, it does not intersect the Miocene deepwater channel, but does provide useful lithology information. Figure 3 shows that the Miocene strata in Romney-1 includes claystone, siltstone, and limestone. SEG polarity convention has been used for seismic data display, i.e., a positive reflection coefficient represents a peak. These lithoelements when tied to the seismic data exhibit strong amplitude, high continuity reflections for limestone to mudstone interfaces, and weaker amplitudes internal to the mudstone deposits. Bright seismic amplitudes seen within the channel are associated with shingled reflections indicating sandy fill during channel migration.

## Conditioning seismic data for attribute analysis

Traditional seismic data are seen to preserve information with a frequency content going up to 50 or 60 Hz at the high end of the bandwidth. While such bandwidths may be acceptable for thicker conventional reservoirs, they could lack the needed resolution and be unacceptable for deepwater turbidite reservoirs. The advancements in seismic data acquisition and processing, coupled with computer capacities and speeds, provide cost-effective solutions for such objectives. For a decade-old vintage seismic dataset we need to apply an amplitude-friendly poststack spectral balancing procedure to enhance the vertical and lateral resolution. The spectral balancing procedure of choice was the method first discussed by Marfurt and Matos (2014), also demonstrated by Chopra and Marfurt (2016).

In this method, data are first decomposed into time-frequency spectral components. Then the power of the spectral magnitude, $P(t,f)=m(t,f)^2$ is averaged over all the traces ($j$ = 1, …$K$) in the data volume spatially and in the given time window, which yields a smoothed average power spectrum, $P_{avg}(t,\ f)$. Next, we compute the peak of the average power spectrum at each time sample, $P_{peak}(t)=MAX\left[P_{avg}(t,\ f)\right]$. Both the average spectral

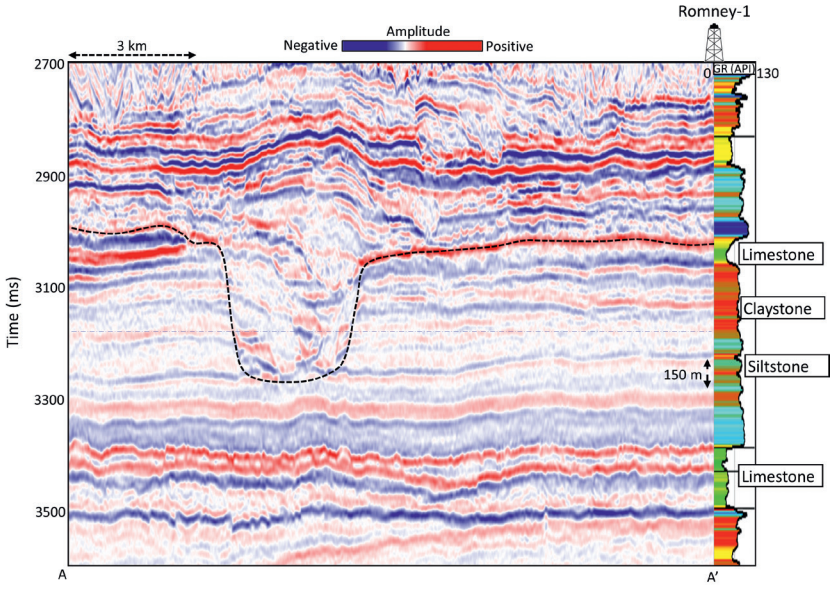


**Figure 3** Line AA' through the seismic amplitude volume showing a deepwater channel. A gamma ray curve has been overlaid on the section at the location of Romney-1 well. The limestone formations exhibit high-amplitude continuous reflections, whereas the claystone and siltstone formations exhibit weaker amplitudes. The moderate amplitude shingled reflections within the channel probably represent more sand-rich facies.

magnitude and the peak of the average power spectrum are used to design a single time-varying spectral-balancing operator that is applied to each and every trace in the data:

$$m_j^{bal}(t,f)=\left[\frac{P_{peak}(t)}{P_{avg}(t,f)+\varepsilon P_{peak}(t)}\right]^{\frac{1}{2}} m(t,f) \quad (1)$$

where $\varepsilon$ is the prewhitening parameter. A conservative value would be $\varepsilon = 0.04$. For larger surveys in which the estimate of the average spectra is statistically more robust, one might use values of $\varepsilon = 0.01$ in many cases, further broadening the spectrum. However, as with any filter, the interpreter needs to determine whether such aggressive spectral balancing introduces ringing in the data. Such spectral balancing is amplitude friendly because a single time-varying wavelet is applied to the entire data volume.

Figure 4a and b shows a comparison of segments of seismic sections traversing the deepwater channel complex before and after frequency balancing, along with their frequency spectra. Notice the well-defined appearance of the reflections both outside and within the channel complex in Figure 4b as well as the flattened appearance of the frequency spectra as compared with the input seismic volume.

This data volume was then put through structure-oriented filtering and attribute computation. To bring out the advantage of frequency balancing and structure-oriented filtering, we compute relevant attributes on the data before and after the two data conditioning processes and compare the results in the next section.

## Coherence attribute

Encouraged with the higher-frequency content of the seismic data, we first generated the coherence attribute. Much has been written about this attribute and the usefulness of its application.

The alternative coherence algorithms vary in how they handle lateral variations in amplitude, phase, and waveform, and thus have different sensitivities to geology, spectral bandwidth, and seismic noise. Whatever the algorithm choice, coherence is best computed along structural dip. A covariance matrix is then constructed from the selected samples and solved, i.e., the eigenvalues and eigenvectors are determined. The ratio of the first eigenvalue (by definition the largest) to the sum of all the eigenvalues is the value of the eigenstructure coherence at the sample at the centre of the unit cube. The analysis window is then shifted by one sample at a time in the inline, crossline and time directions, and the above process repeated. The result is a coherence volume, which is ready for interpretation.

The energy ratio-based coherence algorithm (Chopra and Marfurt, 2008) is a generalization of Gersztenkorn and Marfurt's (1999) eigenstructure-based coherence computation, where the original trace and its Hilbert transform are used to construct the covariance matrix, thereby minimizing artifacts at zero crossings, and thereby providing the ability to use shorter analysis windows resulting in reduced stratigraphic mixing. Coherence run on band-pass filtered or spectral voice components often delineate edges at or near the tuning frequency of a given formation (Chopra and Marfurt, 2019a, 2019b). In general, shorter, more vertically limited faults and channel edges are often better delineated at higher frequencies, while through-going faults are often better delineated at lower frequencies.

In addition to computing a covariance matrix from each band-passed filtered version of the data and then computing coherence for each one, we can also add the covariance matrices and compute coherence from its sum, giving rise to *multispectral coherence* computation (Li and Liu, 2014; Chopra and Marfurt, 2018).

We demonstrate the application of broadband and multispectral coherence on the input and frequency-balanced seismic

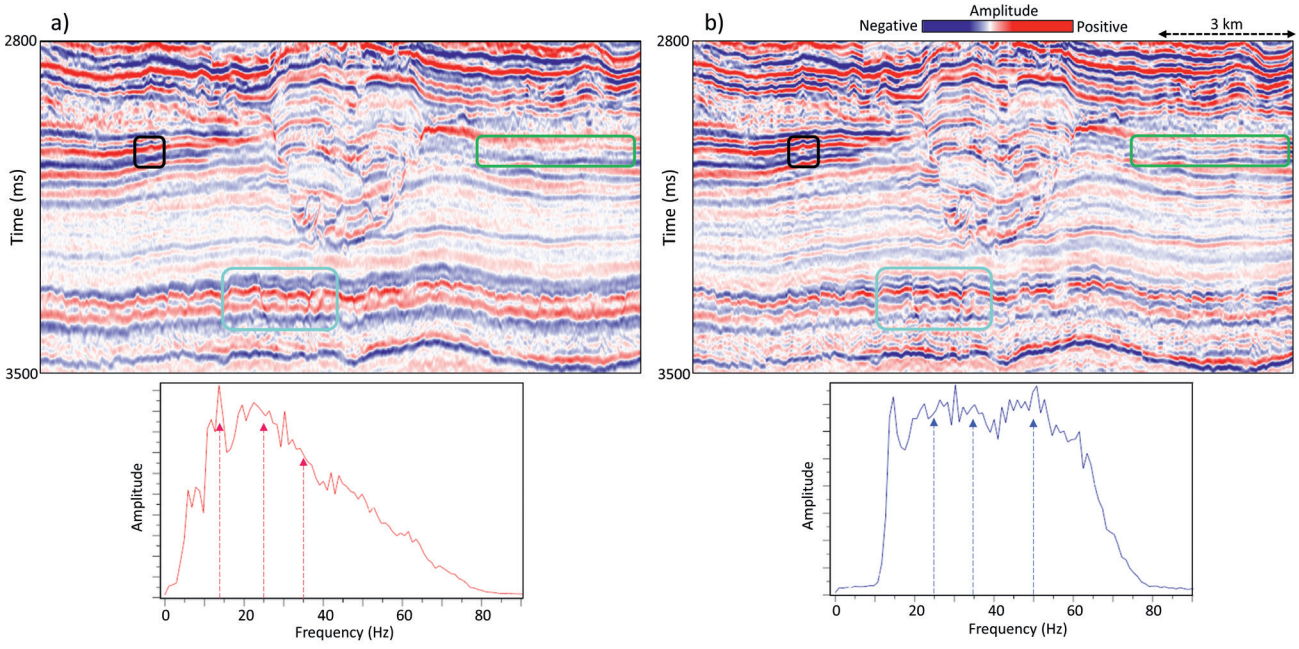


**Figure 4** Line BB' through the seismic amplitude volume and its frequency spectrum (a) before and (b) after spectral balancing resulting in a statistically flatter spectrum. Examining the spectrally balanced image, we notice a small channel inside the black box, greater resolution of thinner reflectors in the green box, and more clearly defined offsets across the faults in the cyan box. In contrast, the steeply dipping fault plane reflectors are more clearly delineated in the cyan box on the unbalanced data. These events exhibit a very low apparent vertical frequency and were reduced by spectral balancing.

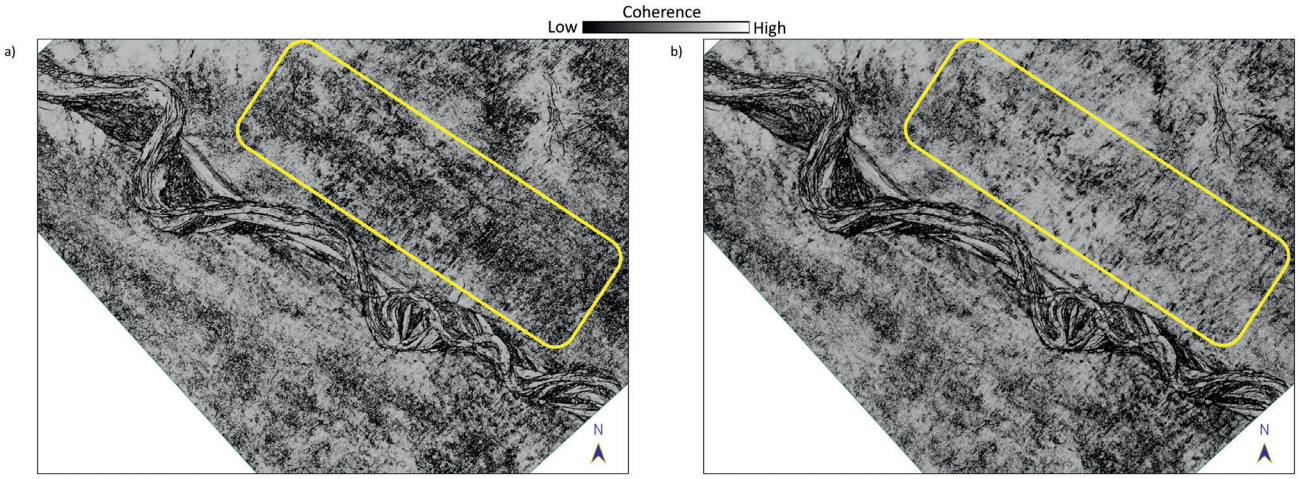


**Figure 5** Time slice at t=3.18 s through the (a) broadband and (b) multispectral coherence volumes. Many of the linear artifacts aligned with the inline direction are suppressed in the multispectral coherence volume. In contrast, although the strong channels features are darker in the multispectral coherence, they are otherwise nearly identical when animated. The time level of the displayed slices on the seismic section in Figure 3 is indicated with a blue dashed line.

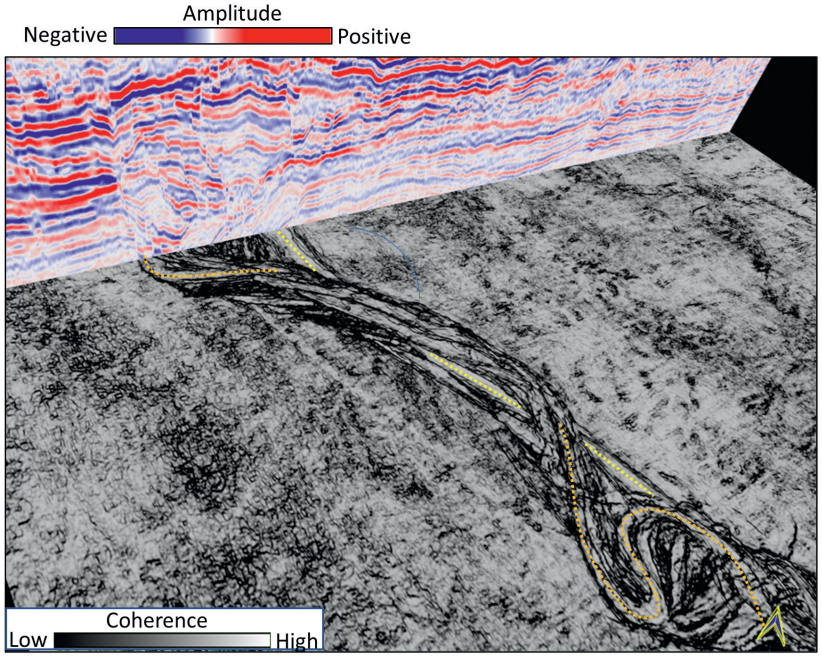


**Figure 6** A chair display showing a vertical seismic section intersecting a time slice through the multispectral coherence volume. The coherence time slice more clearly shows the relation between the channel elements seen on the vertical section, where the meandering orange channel cuts through the earlier, straighter yellow channel. If we hypothesize that greater tortuosity (the ratio of channel length to the straight-line distance to the endpoints) indicates slower flow rates and finer sediment deposition, we have the risk of a shale-rich orange channel compartmentalizing the sandier yellow channel.

data volumes. Figure 5 shows a comparison of time slices at *t*=3.18 s from both coherence volumes. The channel features seen on the multispectral coherence display are well defined overall and therefore very clearly seen and exhibit higher signal-to-noise ratio. The best practice for stratigraphic objectives is to analyse stratal or even geochronostratigraphic slices through the data. In our example the structural dip is low such that the stratal slices are almost parallel to the time slices at the level of the channel. For this reason, we use time slice displays to minimize any bias due to errors in the horizon picking. The chair display shown in Figure 6 shows the seismic signature of the channel complex at different locations along its length.

## Spectral decomposition

Spectral decomposition is a well-established tool that helps in the analysis of subtle stratigraphic plays and fractured reservoirs. It decomposes the broadband seismic data into individual narrow-band frequency components that fall within the measured seismic bandwidth, so that the same subsurface geology can be seen at different frequencies. Tuning is a function of the two-way travel time thickness, and thus depends not only on the thickness measured in metres, but also on lithology, porosity, and fluid content that affect the velocity. Temporally thick beds or features will be tuned and have relatively higher amplitudes at lower frequencies, while temporally thinner beds will be tuned and have relatively higher amplitudes at higher frequencies.

Spectral magnitude highlights features that are tuned, and the phase components enhance subtle faults and channel edges that can be used as input to subsequent seismic attribute analysis, such as coherence. There are different methods for computing spectral decomposition, namely, the traditional short-window discrete Fourier transform (Partyka et al., 1999), continuous wavelet transform (Sinha et al., 2005), S-transform (Stockwell et al.,1996), and matching pursuit (Mallat and Zhang, 1993) methods. In this work we employ the matching pursuit method, which is known for producing high-resolution attributes.

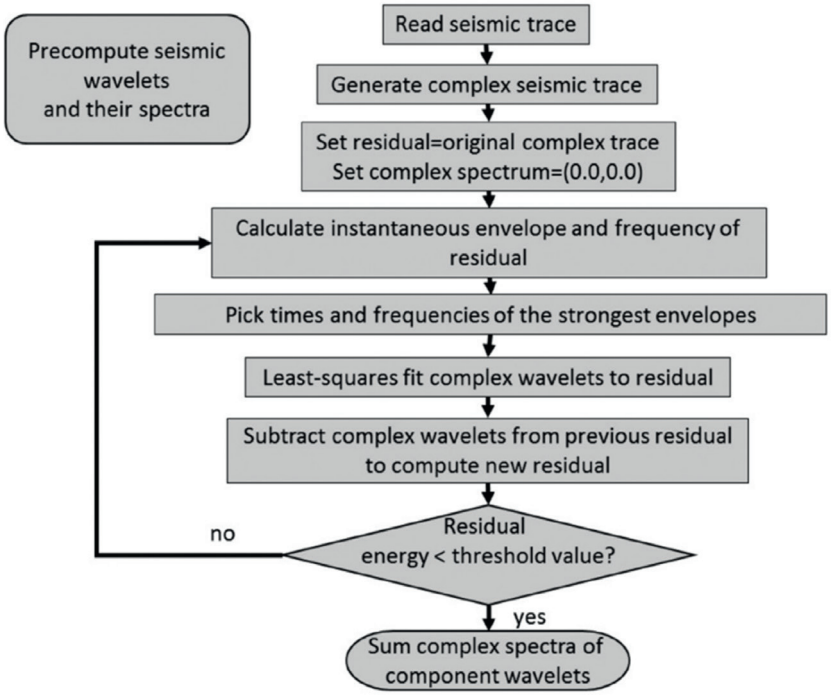


**Figure 7** The complex matching pursuit workflow. *(After Liu and Marfurt, 2007).*

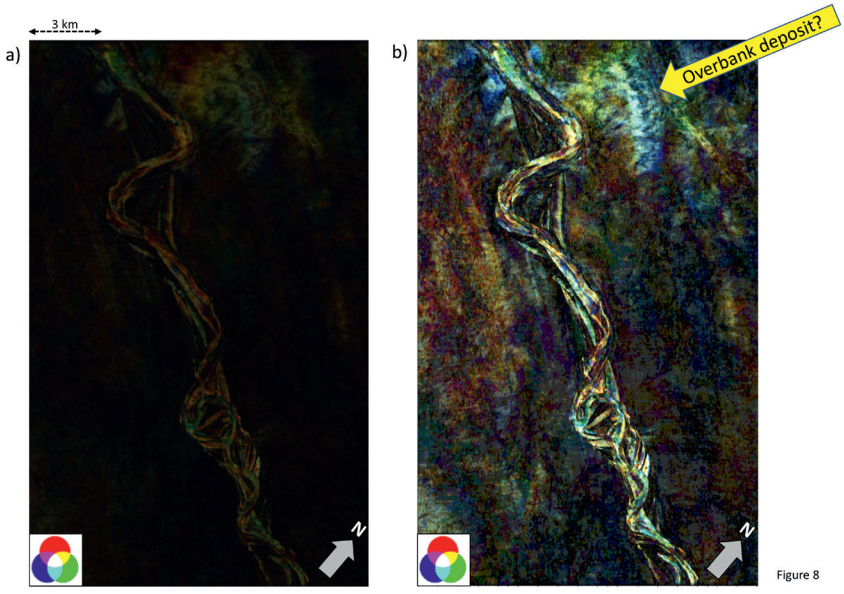


**Figure 8** Time slice at 3.18 s from RGB corendered spectral magnitude on (a) input seismic volume, and (b) on frequency-balanced seismic volume at 25 Hz, 35 Hz, and 50 Hz. Note the clear disposition and definition of the channel complex in (b).

The idea behind a matching pursuit algorithm is that the bandlimited seismic trace is composed as a superposition of a discrete number of source wavelets (sometimes called 'atoms'). Each Morlet or Ricker wavelet used has a well-defined spectrum; thus, by finding the constituent wavelets that fit the data we also compute the spectra at each time sample. There are several ways of computing matching pursuit decomposition; here, we follow the Liu and Marfurt (2007) workflow, which is summarized in Figure 7.

Clearly, the imprint of the seismic source wavelet affects the spectral magnitude slices, overprinting any tuning effects. For this reason, a best practice is to spectrally flatten the data using a statistical method similar to that in equation 1, or a more deterministic method such as spectral shaping using an estimate of the source wavelet obtained with the aid of well logs. Figure 8 shows the corendered spectral magnitudes computed at 25, 35, and 50 Hz without and with spectral balancing. Not surprisingly, Figure 8a shows mostly red, yellow, and green; Figure 8b shows cyan and blue as well. Most commercial workstation software will allow the interpreter to interactively scale the value of each spectral component, thereby approximating the spectral balancing of equation 1, but without the constraints of vertically smoothing the spectrum and adding a prewhitening factor, making the process quite subjective.

Changing the amplitude of a given spectral voice component (bandpass-filtered version of the data) for the entire survey has little impact on coherence, which is sensitive only to lateral changes in amplitude. However, because the different spectral components see the channel edges at different frequencies, corendering the coherence computed at 25, 35, and 50 Hz provides a measure of the temporal thickness of a given edge (Figure 9).


**Figure 9** Time slice at 3.18 s through the CMY corendered coherence volumes computed at 25 Hz (against cyan), 35 Hz (against magenta), and 50 Hz (against yellow). Coherence anomalies that are stronger at lower frequencies indicate thicker edges, while those stronger at higher frequencies indicate thinner edges. Coherence anomalies that are the same for all frequencies appear as black.

## Sweetness attribute

Sweetness is a 'meta-attribute' (Radovich and Oliveros, 1998) or one computed from others, which **in** this case is the ratio of the envelope and the square root of the instantaneous frequency. In many Tertiary Basins, a clean sand embedded in a shale will exhibit high envelope and lower instantaneous frequency, and thus higher sweetness, than the surrounding shale-on-shale reflections.

Hart (2008) showed applications of sweetness attribute in imaging sand-filled channels from both deep-water and fluvial-systems embedded in shale formations. This becomes possible in marine clastic settings where the shale-dominated intervals exhibit low amplitudes (small impedance contrast) and higher frequencies due to relatively closely spaced reflections, whereas sandy intervals such as channel fills and frontal splays in shales are associated with higher amplitudes (high impedance contrast) and lower frequencies (due to broad reflections). The sandstones correspond to high sweetness when the impedance contrast with the shale is high. Sweetness may not be useful for other lithologies when the contrast is low.

If the data are not spectrally balanced, such as shown in the spectrum of Figure 4a, the range of the instantaneous frequency used in the sweetness attribute will be biased to the low end of the spectrum. In contrast, spectral balancing results in instantaneous frequency values that range from 10 to 60 Hz, thereby increasing the dynamic range, and hence lateral resolution of the sweetness attribute.

Figure 10 shows a comparison of time slices at 3.18 s through the sweetness attribute computed on the input seismic volume (Figure 10a) and the equivalent slice through sweetness computed on frequency-balanced seismic volume (Figure 10b). Both displays are shown corendered with coherence. Notice the better sweetness definition both within and outside the channel complex in Figure 10b.

## Relative acoustic impedance

Relative acoustic impedance is computed by continuous integration of the original seismic trace with the subsequent application of

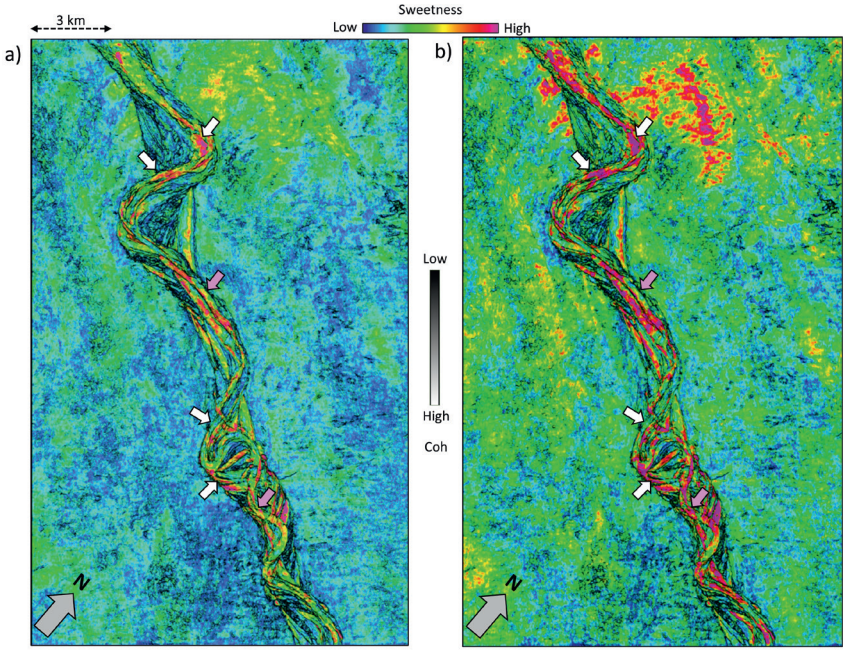


**Figure 10** Time slices at t=3.18 s from sweetness attribute computed on (a) input seismic volume and the equivalent slice from sweetness computed on (b) frequency-balanced seismic volume. Both displays are shown corendered with coherence. Notice the better sweetness definition both within and outside the channel complex in (b).

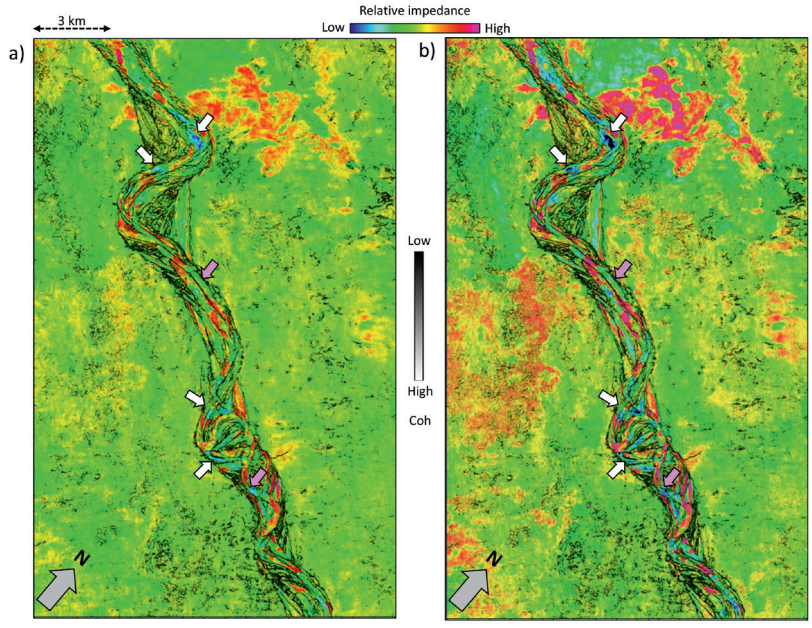


**Figure 11** Time slices at 3.18 s from relative impedance attribute computed on (a) input seismic volume and the equivalent slice from relative impedance computed on (b) frequency-balanced seismic volume. Both displays are shown corendered with coherence. Notice the better sweetness definition both within and outside the channel complex in (b).

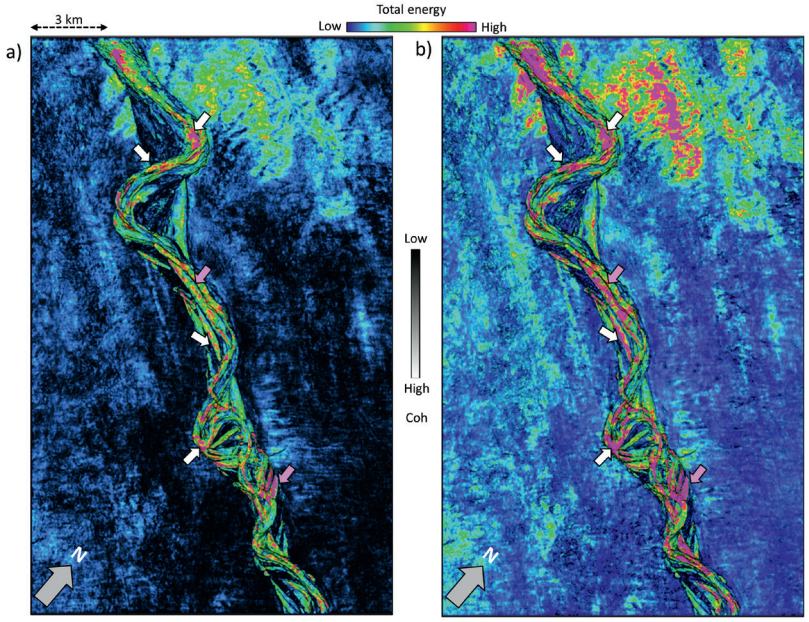


**Figure 12** Time slices at 3.18 s from total energy attribute computed on (a) input seismic volume and the equivalent slice from total energy computed on (b) frequency-balanced seismic volume. Both displays are shown corendered with coherence. Notice the better sweetness definition both within and outside the channel complex in (b).

low-cut filter. The impedance transformation of seismic amplitudes enables the transition from reflection interface to interval properties of the data, without the requirement of a low-frequency model. Figure 11 shows a comparison of time slices at t=3.18 s through relative impedance computed on the input seismic volume (Figure 11a) and the equivalent slice through relative impedance computed on frequency-balanced seismic volume (Figure 11b). Both displays are shown corendered with coherence. Notice the better relative impedance definition both within and outside the channel complex in Figure 11b.

## Total energy

The total energy attribute helps to isolate low energy chaotic reflectors from higher energy seismic responses. It is computed by measuring the energy associated with the sum of eigenvalues computed from the covariance matrix of the windowed seismic traces (Gersztenkorn and Marfurt, 1999). Figure 12 shows a comparison of time slices at 3.18 s from total energy computed on the input seismic volume (Figure 12a) and the equivalent slice from total energy computed on frequency-balanced seismic volume (Figure 12b). Both displays are shown corendered with coherence. Notice the better total energy definition both within and outside the channel complex in Figure 12b.

## Reflector convergence

We next consider the computation of a relatively less common volumetric attribute called reflector convergence, which is useful in the interpretation of angular unconformities. It is a measure of the change in reflector normal about a horizontal axis. This attribute can facilitate and quantity the use of seismic stratigraphic workflows to large 3D seismic volumes.

Because of the distinct change in reflector dip and/or terminations, erosional unconformities and in particular angular unconformities are relatively easy to recognize on vertical seismic

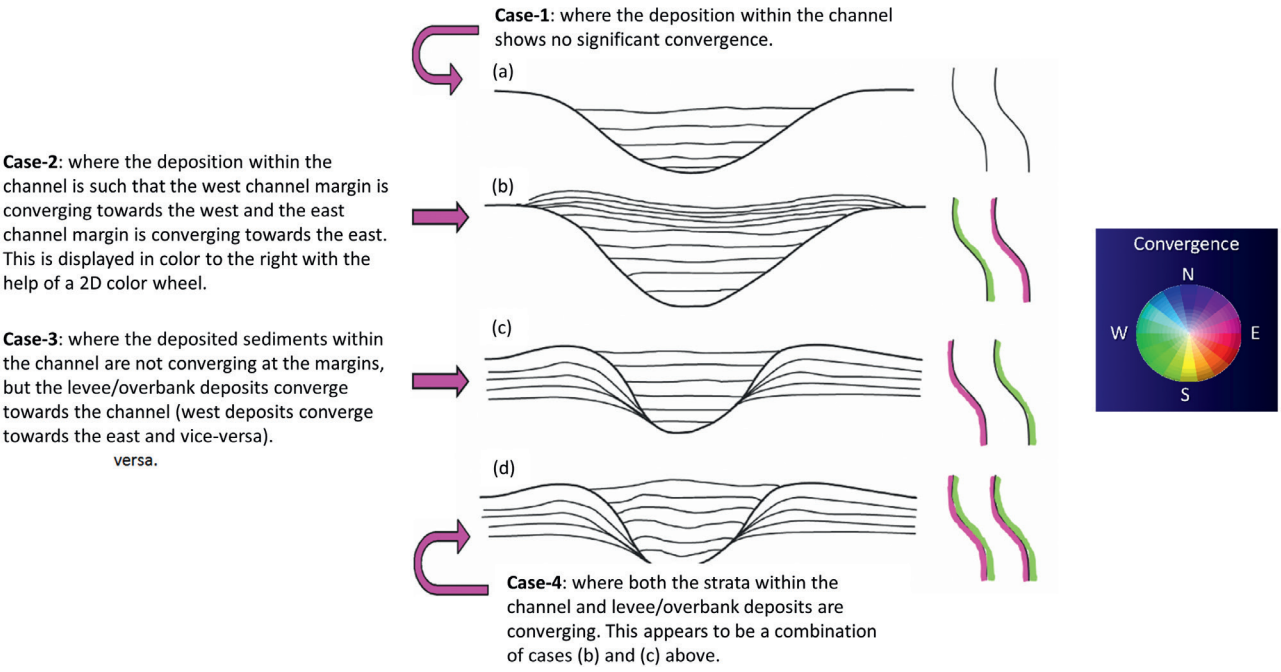


**Figure 13** Cartoons demonstrating convergence within a channel with or without levee/overbank deposits. (Interpretation courtesy: Supratik Sarkar) (After Chopra and Marfurt, 2013).

sections. Although low-coherence anomalies often appear on time slices where reflectors of conflicting dip intersect, these anomalies take considerable skill to interpret. Barnes (2000) introduced an attribute that maps such unconformities volumetrically by computing the mean and standard deviation of the vector dip within local windows. Stratigraphic facies exhibiting parallelism have a small standard deviation, facies that pinch out may have a moderate standard deviation, and facies that are chaotic often have a high standard deviation.

Computing a vertical derivative of apparent dip along a user-defined azimuth, Barnes (2000) also computed the convergence and divergence of reflections. As reflection divergence is characterized by increasing reflection dip, and likewise reflection convergence by decreasing reflection dip with depth, in 2D, converging reflectors exhibit a decrease in dip p with depth ($dp/dx < 0$) while diverging reflectors exhibit an increase in p with depth ($dp/dx > 0$).

Marfurt and Rich (2010) built upon Barnes' (2000) method by volumetrically computing the curl, $\Psi$, of the unit length vector perpendicular to the reflector, or unit normal, $\hat{\mathbf{n}}$:

$$\Psi = \nabla \hat{\mathbf{n}} = \hat{\mathbf{x}}\left(\frac{\partial n_y}{\partial z} - \frac{\partial n_z}{\partial y}\right) + \hat{\mathbf{y}}\left(\frac{\partial n_z}{\partial x} - \frac{\partial n_x}{\partial z}\right) + \hat{\mathbf{z}}\left(\frac{\partial n_x}{\partial y} - \frac{\partial n_y}{\partial x}\right) \quad (2)$$

where the unit normal vector has three components, $n_x$, $n_y$, and $n_z$ and the circumflex indicates the unit normals along the *x, y*, and *z* axes.

Components of this curl vector perpendicular to the average (usually close to vertical) reflector normal, $\bar{\boldsymbol{n}}$, measure reflector convergence North and East components, or alternatively reflector convergence azimuth and magnitude:

$$\mathbf{c} = \bar{\mathbf{n}} \times \Psi \quad (3)$$

Figure 13 illustrates seismic stratigraphic patterns or 'reflector convergence' within a channel with and without levee/overbank deposits. Notice how the convergence shows up in colour (using the 2D colour wheel) as displayed to the right in green and magenta colours along the channel edges.

Figure 14 shows a comparison of time slices at t=3.18 s through reflector convergence computed on the input seismic volume (Figure 14a) and the equivalent slice through reflector convergence computed on frequency-balanced seismic volume (Figure 14b). Both displays are shown corendered with coherence. Notice the better reflector convergence definition both within and outside the channel complex in Figure 14b.

In Figure 15 we show a segment of a vertical section from the seismic data volume depicting the main channel signature, and we try and correlate the individual signatures with the channel definition seen on the multispectral coherence time slice at t=3.18 s. This level is shown with a dotted line on the seismic display. Notice how the original channel position is marked with a black dashed outline and has been shown correlated with the channel definition on the coherence display. The gradual lateral migration of the channel can also be interpreted as shown with the red dashed lines on both the seismic and coherence displays. Similarly, the present-day position of the channel levees is shown with cyan dashed lines on both displays. Thus, the coherence attribute helps interpret the original position of the channel as well as its lateral migration up to the present-day position. In addition, the equivalent attribute vertical displays as labelled, corendered with the seismic amplitudes in grey scale, have been included in the display. The individual attributes pick up different features of the channel architecture, and we expect all such component features to come together when we churn through them in machine learning applications discussed next.

## Machine learning applications used for unsupervised seismic facies classification

Machine learning uses mathematical operations to learn from the similarities and differences in the provided data and make predictions. Besides the supervised and deep learning machine learning techniques, there are two broad families of unsupervised machine learning algorithms. The *first* algorithm family includes dimensionality reduction algorithms such as PCA and ICA (Chopra et al., 2018; Chopra and Marfurt, 2018) where $N \geq 3$ attribute volumes are represented by two or three component volumes. When plotted against a 2D or 3D colour bar, the interpreter may be able to identify clusters, but the algorithm output is a continuum of data projected onto the lower dimensional hyperplane. The *second*, unsupervised classifica-

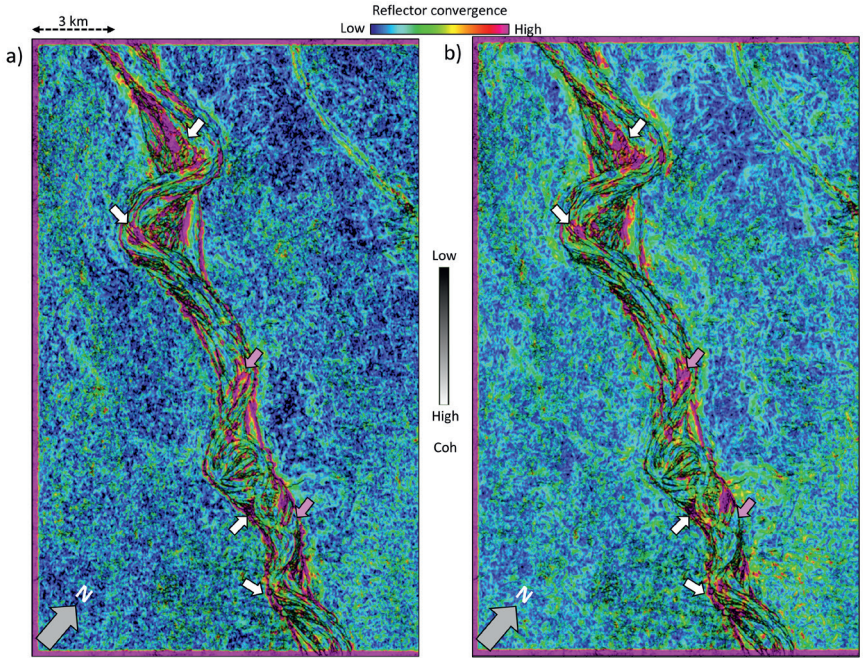


**Figure 14** Time slices at 3.18 s from reflector convergence attribute computed on (a) input seismic volume and the equivalent slice from reflector convergence computed on (b) frequency-balanced seismic volume. Both displays are shown corendered with coherence. Notice the better sweetness definition both within and outside the channel complex in (b).

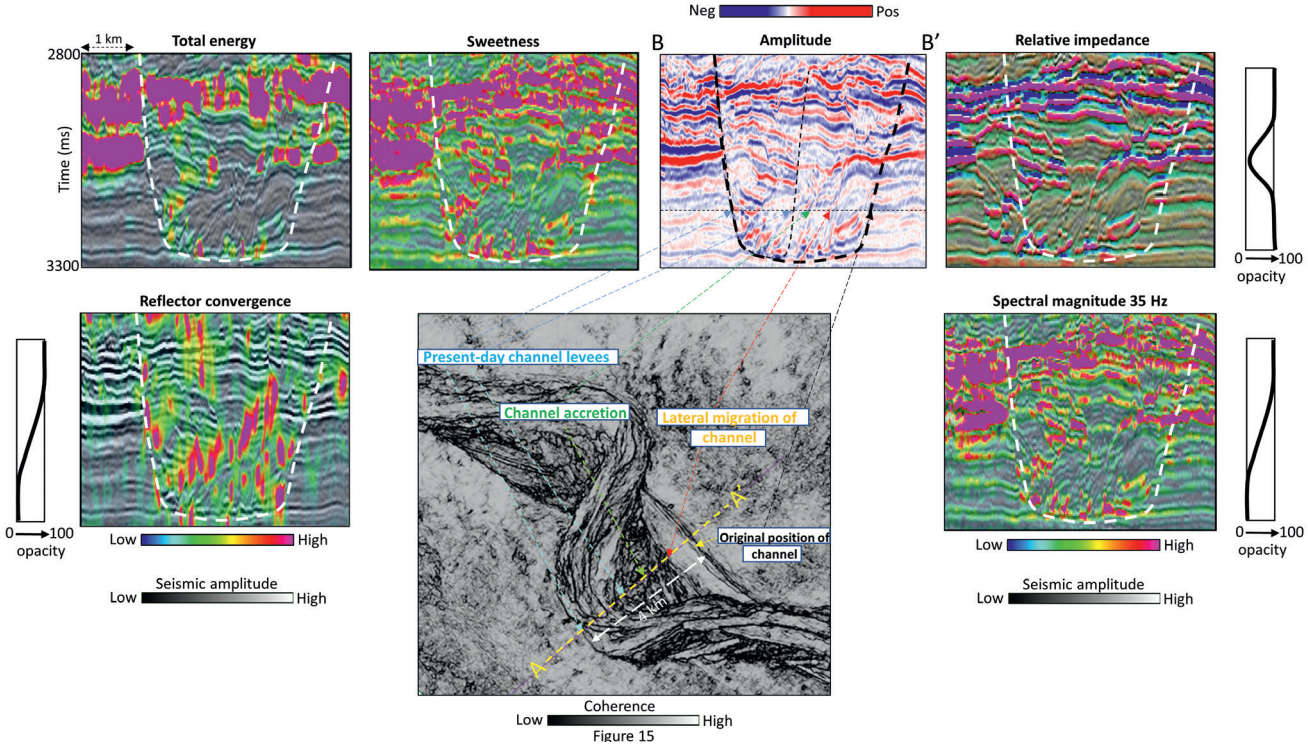


Figure 15

**Figure 15** (Middle) Time slice at 3.18 s from multispectral coherence volume shows the main channel architecture clearly. Vertical seismic sections from seismic data as well as the derived attribute volumes are shown above. The signature of the original position of the channel is shown on the vertical sections with a dashed outline (black on the seismic and white on the attribute volumes). How the original position of the channel migrates laterally, the channel accretion as well as the present-day channel position are marked on the coherence slice, and their seismic signatures are also pointed with the arrows. The attribute data are shown corendered, with the seismic amplitudes in grey scale using transparency setting the low values as transparent and high values opaque. For relative impedance, the values close to zero are set as transparent and the extreme values opaque as indicated.

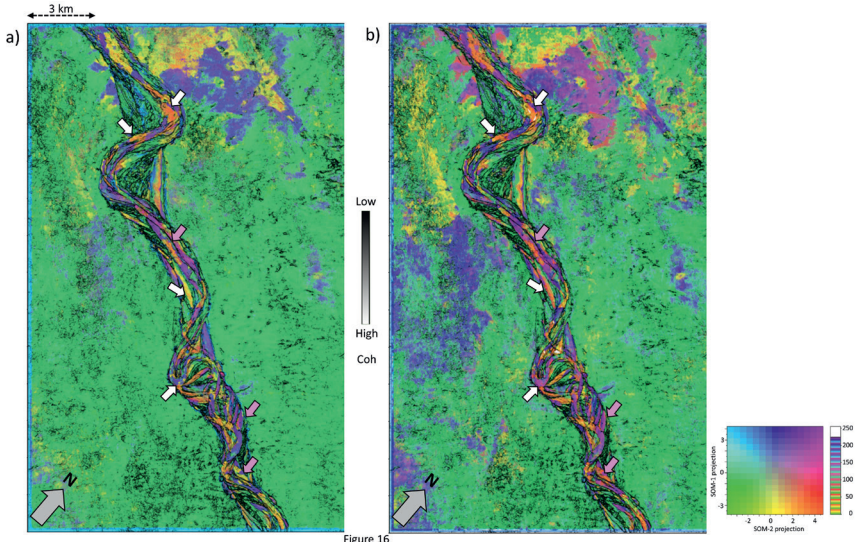


Figure 16

**Figure 16** Time slices at 3.18 s from SOM1-versus-SOM2 crossplot volume computed on (a) input seismic volume and the equivalent slice from SOM1-versus-SOM2 crossplot volume computed on (b) frequency-balanced seismic volume. Both displays are shown corendered with coherence. Notice the better sweetness definition both within and outside the channel complex in (b) as indicated by block arrows.

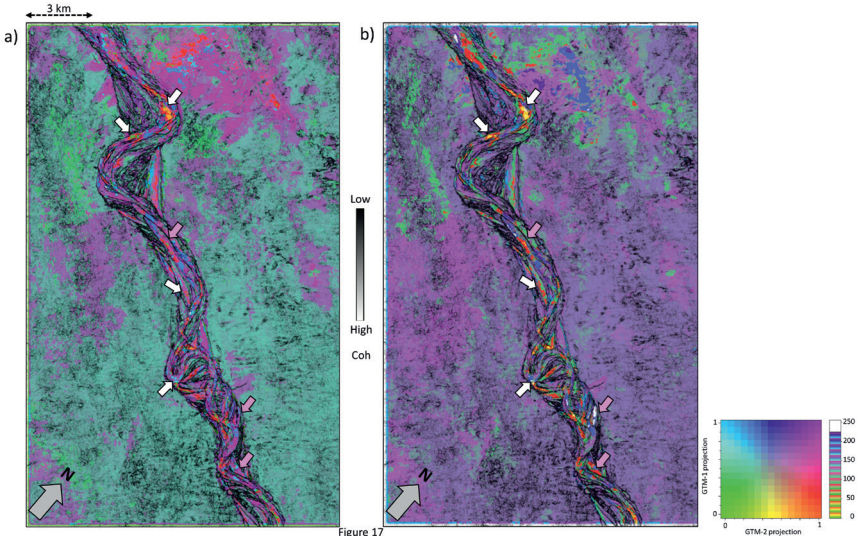


Figure 17

**Figure 17** Time slices at 3.18 s from GTM1-versus-GTM2 crossplot volume computed on (a) input seismic volume and the equivalent slice from GTM1-versus-GTM2 crossplot volume computed on (b) frequency-balanced seismic volume. Both displays are shown corendered with coherence. Notice the better sweetness definition both within and outside the channel complex in (b) as indicated by black arrows.

tion algorithm family attempts to explicitly cluster the data into a finite number of groups that in some metric 'best represent' the data provided. Two methods that fall under this category are the self-organizing mapping (SOM) and generative topographic mapping (GTM). In both algorithms the data are represented by neurons that lie on a deformed 2D or 3D manifold that fits the *N*-dimensional data where each attribute represents a dimension. In this manner, clusters that are near each other in *N*-dimensions will also be near each other when projected onto the deformed manifold. We show the application of both these methods to the Romney 3D seismic volume, on both the input and frequency balanced versions.

## Self-organizing maps

Self-organizing mapping (SOM) is a technique that generates a seismic facies map from multiple seismic attributes, in an unsupervised manner. It defines its initial cluster centroids in an N-dimensional attribute data space and uses the first two eigenvectors of the covariance matrix to least-squares fit the data with a plane (Kohonen, 1982, 2001). Grid prototype vectors (also called neurons) defined in this plane, are attracted to data out of the plane, deforming it into a 2D surface called a manifold that better fits the data. After convergence, the N-dimensional data are projected onto this 2D surface and are in turn mapped against a 2D plane or 'latent' (hidden) space defined by axes SOM-1 and SOM-2, in which the interpreter either explicitly defines clusters by drawing polygons, or implicitly defines clusters by plotting the results against a 2D colour bar. Matos et al., (2003, 2004, 2007) and Zhao et al. (2015) describe the details of the SOM method and demonstrate its application for seismic facies classification on data from different basins.

Figure 16 shows the equivalent time slice (t=3.18 s) to those shown earlier, extracted from the crossplot volume generated between the SOM-1 and SOM-2 volumes using a 2D colour bar shown alongside. Figure 16a shows the display for the SOM computation carried out when the input attributes were computed on the input seismic data volume were used, and Figure 16b displays the equivalent display when the attributes were computed on the frequency balanced seismic data. The features seen on the display in Figure 16b are better defined in terms of more colour separation and distinct definition than the ones seen in Figure 16a.

## Generative topographic mapping

Although popular as an unsupervised clustering technique for its straightforward implementation and its low computation cost, the Kohonen self-organizing map has limitations. There is no theoretical basis for selecting the training radius, neighbourhood function and learning rate as these parameters are data dependent (Bishop et al., 1998; Roy, 2013). No cost function is defined that could be iteratively minimized which would indicate the convergence of the iterations during the training process, and finally no probability density is defined that could yield a confidence measure in the final clustering results. Bishop et al. (1998) developed an alternative technique called a generative topographic mapping (GTM) algorithm that provides a probabilistic representation of the data vectors in latent space.

The GTM method begins with an initial array of $K$ grid points $\mathbf{m}_k$ arranged on an initial estimate of the manifold providing the first two or three principal components or the ICA components. Each of the grid points are then nonlinearly mapped onto a two- or three-dimensional latent space. The likelihood of any data point $\mathbf{x}_r$ being represented by the $k^{th}$ grid point is defined by an $N$-dimensional Gaussian function centered about a midpoint $\mathbf{m}_k$ with a fixed variance $1/\beta$. At each iteration, the variance $1/\beta$ is decreased and the Gaussian centroids $\mathbf{m}_k$ moved to better represent the data (in a process called expectation maximization) until we reach convergence. Unlike SOM which assigns a data point to best matching neuron (or cluster), GTM measures the probability that any data point is represented by each of the cluster centres, thereby providing a measure of how confident we are in assigning it to one or more clusters. Roy (2013) and Roy et al. (2014) describe the details of the method and demonstrate its application for mapping of seismic facies to the Veracruz Basin, Mexico.

In our example, the SOM and GTM techniques project data from a higher dimensional space (7D when seven attributes are used) to a lower 2D dimensional deformed surface. Once they are projected onto a lower dimensional space, the data can be clustered and assigned to the most representative neuron. When the SOM model is overparameterized by say 256 neurons, the neurons will clump together to represent the number of seismic facies (including noise facies) in the data and be displayed by nearly identical colours. We find it most valuable to interactively cluster the neurons (or for GTM, the Gaussian centres) using polygons drawn on the 2D latent space.

After the application of GTM to the data at hand, Figure 17 shows the equivalent stratal display to the ones shown earlier, extracted from the crossplot volume generated with GTM-1 and GTM-2 volumes using the 2D colour bar shown alongside. Figure 17a shows the display for the GTM computation carried out when the input attributes were computed from the original seismic data volume. Figure 17b displays the equivalent display when the attributes were computed on the frequency balanced seismic data. Clusters seen on the display in Figure 17b are better defined in terms of more colour separation and distinct definition, than the ones seen in Figure 17a.

## Discussion

The choice of attributes in machine learning depends on the features we wish to delineate. Common objectives may include mapping of seismic facies, or the internal character of a package of sediments, or the mapping of faults and channel edges. Some attributes can be used to map both, with coherence being able to highlight the chaotic internal reflectivity or low signal-to-noise ratio of salt diapirs and karst collapse as well as stratigraphic and structural edges. Similarly, spectral magnitude components often exhibit low values near faults, either because the data are scattered or because the reflectivity of fault plane reflectors map is mapped to lower apparent frequencies. Reflector convergence can exhibit both the gentle thinning and thickening of sediments or the abrupt change in dip about angular unconformities and deeper part of listric faults. In this work we have chosen to use coherence to delineate the edges of the clusters computed from attributes more sensitive to the internal character of the seismic facies through simple corendering rather than as input to the machine learning algorithms.

## Conclusions

The seismic attribute computation carried out on the input seismic data as well as the frequency-balanced seismic have shown more detailed definition of the channel complex features on the latter. Some of these attributes have revealed channel details not seen earlier.

The workflow adopted for carrying out seismic facies classification through unsupervised machine learning by way of SOM and GTM application has clearly indicated the lateral variability of the channel complex, with the GTM approach having an edge over SOM.

Though the analysis is qualitative at present, it paves the way for more detailed work as more well and other data become available.

## Acknowledgements

The first author would also like to thank the Geomodeling Technology Corporation for making the Attribute Studio software available, which has been used for some visualization displays shown in this paper, as well as the Attribute-Assisted Seismic Processing and Interpretation Consortium, University of Oklahoma, for access to their software, which has been used for all attribute computation. The authors would like to thank the FB editor, Angelika Wulff for making good suggestions which improved the quality of the manuscript during the review process.

## References

Barnes, A.E. [2000]. Attributes for automated seismic facies analysis: 70th Annual International Meeting, SEG, Expanded Abstracts, 553–556, http://dx.doi.org/10.1190/1.1816121.

Bishop, C.M., Svensen, M. and Williams, C.K.I. [1998]. The generative topographic mapping: *Neural Computation*, **10**(1), 215-234.

Braccini, E., and Adeyemi, A. [2011]. Integrating seismic attributes for geomodelling purposes: Nigeria deep water turbidite environment case study: GCSSEPM 31st Annual Bob. F. Perkins Research Conference on Seismic attributes – New views on seismic imaging: Their use in exploration and production, 259-283.

Chopra, S. and Marfurt, K. J. [2008]. Gleaning meaningful information from seismic attributes: *First Break*, **26**(9), 43-53, http:// dx.doi.org/10.3997/1365-2397.2008012.

Chopra, S. and Marfurt, K.J. [2013]. Volumetric estimates of seismic reflector rotation and convergence — Tools for mapping rotation about faults and seismic stratigraphy: *The Leading Edge*, **32**, 402-408.

Chopra, S. and Marfurt, K.J. [2016]. Spectral decomposition and spectral balancing of seismic data: *The Leading Edge*, **35**, 176-179.

Chopra, S. Marfurt, K.J. [2018]. Multispectral, multiazimuth, and multioffset coherence attribute applications: *Interpretation*, **7**(2), SC21-SC32. http://dx.doi.org/10.1190/INT-2018-0090.1.

Chopra, S., Lubo-Robles, D. and Marfurt, K.J. [2018]. Some machine learning applications in seismic interpretation*: AAPG Explorer*, August issue, **39**, 22-24.

Chopra, S. and Marfurt, K.J. [2018] Seismic facies classification using some unsupervised machine learning methods: 88th Annual International Meeting, SEG, Expanded Abstracts, 2056-2060.

Chopra, S. and Marfurt, K.J. [2019]. Coherence attribute applications on seismic data in various guises — Part 1: *Interpretation*, **6**(3), T521-T529. http://dx.doi.org/10.1190/INT-2018-0006.1.

Chopra, S. and Marfurt, K.J. [2019]. Coherence attribute applications on seismic data in various guises — Part 2: *Interpretation*, **6**(3), T531-T541. http://dx.doi.org/10.1190/INT-2018-0007.1.

Deepwater GOM production available at
https://geographic.org/deepwater_gulf_of_mexico/production_rates.html accessed on 15 July, 2022.

Deptuck, M.E. [2003]. Post-rift geology of the Jeanne d'Arc Basin, with a focus on the architecture and evolution of early Paleogene submarine fans, and insights from modern deep-water systems: Ph.D. Thesis, Dalhousie University, Halifax, NS, Canada.

Gersztenkorn, A. and Marfurt, K.J. [1999]. Eigenstructure-based coherence computations as an aid to 3-D structural and stratigraphic mapping: *Geophysics*, **64**, 1468-1479.

Grahame, J. [2015]. Deepwater Taranaki Basin, New Zealand – New Interpretation and Modelling Results for Large Scale Neogene Channel and Fan Systems: Implications for Hydrocarbon Prospectivity, AAPG Search and Discovery Article #10822, accessed on 24th June 2022.

Hart, B. [2008]. Channel detection in 3D seismic data using sweetness: *AAPG Bull*., **92**(6), 733-742.

Kohonen, T. [1982]. Self-organized formation of topologically correct feature maps: *Biological Cybernetics*. **43**, 59-69.

Kohonen, T. [2001]. Self-organizing Maps: Springer-Verlag.

Liu, J.L. and Marfurt, K.J. [2007]. Multi-colour display of spectral attributes: *The Leading Edge*, **26**, 268–271, http://dx.doi.org/10.1190/1.2715047.

Li, F.Y. and Lu, W.K. [2014]. Coherence attribute at different spectral scales: *Interpretation*, **2**(1), SA99–SA10. http://dx.doi.org/10.1190/INT-2013-0089.1.

Mallat, S. and Zhang, Z. [1993] Matching pursuit with time-frequency dictionaries: *IEEE Transactions on Signal Processing*, **41**, 3397-3415.

Marfurt, K.J. and Rich, J. [2010]. Beyond curvature — Volumetric estimates of reflector rotation and convergence: 80th Annual International Meeting, SEG, Expanded Abstracts, 1467-1472.

Marfurt, K. and Matos, M. [2014]. Am I blue? Finding the right (spectral) balance: *AAPG Explorer*, http://www.aapg.org/publications/news/explorer/column/articleid/9522/am-i-blue-finding-the-right-spectral-balance, accessed 12 March 2015.

Matos, C.M., Osorio, P.L.M. and Johann, P.R.S. [2003]. Using Wavelet transform and self-organizing maps for seismic reservoir characterization of a deep-water field, Campos basin, Brazil, EAGE 65th Conference & Exhibition.

Matos, C.M., Osorio, P.L.M. and Johann, P.R.S. [2004]. Unsupervised Seismic Facies Classification Using Matching Pursuit and Self Organizing Maps, EAGE 66th Conference & Exhibition.

Matos, M.C., Osorio, P.L.M. and Johann, P.R.S. [2007]. Unsupervised seismic facies analysis using wavelet transform and self-organizing maps: *Geophysics*, **72**, P9-P21.

Mitchell, P., Paez, R., Johnston, D., Mohler, G. and da Cunha Neto, C. [2009]. 4D seismic in deep water at the Dikanza Field, offshore Angola, West Africa, SEG Abstract, 3924-3928.

Partyka, G.A., Gridley, J. and Lopez, J. [1999]. Interpretational applications of spectral decomposition in reservoir characterization: *The Leading Edge*, **18**, 353-360, doi: 10.1190/1.1438295

Radovich, B.J. and Oliveros, R.B. [1998] 3D sequence interpretation of seismic instantaneous attributes from the Gorgon Field: *The Leading Edge*, **17**, 12861293.

Reijenstein, H.M., Posamentier, H.W. and Bhattacharya, J.P. [2011]. Seismic geomorphology and high-resolution seismic stratigraphy of inner-shelf fluvial, estuarine, deltaic, and marine sequences, Gulf of Thailand: AAPG Bulletin, **95**, 1959-1990.

Roy, A. [2013]. Latent space classification of seismic facies: Ph.D. Dissertation, The University of Oklahoma, 212 p.

Roy, A., Romero-Pelaez, A.S., Kwiatkowski, T.J. and Marfurt, K. [2014]. Generative topographic mapping for seismic facies estimation of a carbonate wash, Veracruz Basin, southern Mexico: *Interpretation*, **2**, SA31-SA47.

Sherwood, A. [2002]. New Zealand's exploration potential, Offshore, available at https://www.offshore-mag.com/geosciences/article/16759750/new-zealands-exploration-potential and accessed on 24th June 2022.

Sinha, S., Routh, P., Anno, P. and Castagna, J. [2005]. Spectral decomposition of seismic data with continuous-wavelet transform: *Geophysics*, **70**(6), P19-P25.

Stockwell, R.G., Mansinha, L. and Lowe, R.P. [1996]. Localization of the complex spectrum: the S-transforms: *IEEE Transactions on Signal Process*, **44**(4), 998-1001.

Strogen, D.P., Bland, K.J., Baur, J.R. and King, P.R. [2012]. Regional paleogeography and implications for petroleum prospectivity, Taranaki Basin, New Zealand: Search and Discovery Article #10432, available at https://www.searchanddiscovery.com/pdfz/documents/2012/10432strogen/ndx_strogen.pdf.html, accessed on June 21, 2022.

Uruski, C., Baillie, P. and Stagpoole, V. [2003]. Development of the Taranaki Basin and comparisons with the Gippsland Basin: implications for deepwater exploration: *APPEA Journal*, **43**(1), 185-196.

Uruski, C. and Clark, L. [2009]. NZ deepwater basins boast big oil potential, Scientist, available at https://www.rigzone.com/news/oil_gas/a/84513/nz_deepwater_basins_boast_big_oil_potential_scientist_says/ and accessed on 24 June, 2022.

Xu, E.X., Jin, Y., Coyle, S., Tiwary, D., Posamenthier, H., Royle, A. and Zhang, Z. [2020]. Meet West Africa deep exploration challenge with geomorphology and targeted amplitude variation with offset inversion, Interpretation, 8(1), SA25-SA33. http://dx.doi.org/10.1190/INT-2019-0045.1.

Zhao, T., Jayaram, V., Roy, A. and Marfurt, K.J. [2015]. A comparison of classification techniques for seismic facies recognition*: Interpretation*, **3**, SAE29-SAE58.